Visualizing turbulence anisotropy in the spatial domain with componentality contours

By M. Emory AND G. Iaccarino

1. Motivation and objectives

Visual representations of quantitative information have proven very useful in the context of fluids engineering. In experiments Schlieren imagery for compressible flows and dye/smoke streaks for low-speed flows (Van Dyke 1982) are vivid examples of how physical behaviors and important system dynamics can be observed, giving the analyst a better understanding of the flow structures. Computational fluid dynamics (CFD) relies just as heavily on visual representations to extract understanding from and explore the large amounts of data generated by numerical simulations. Whether using the Q-criterion (Dubief & Delcayre 2000) to investigate vortices or plotting of velocity profiles, the ability to visually represent quantitative data is a critical aspect of numerical simulation analysis.

One such frequently visualized quantity is the anisotropic behavior of turbulence, a common feature of complex fluid flows. In many engineering applications, properly predicting the amount and type of anisotropy is critical for accurate numerical simulation of these flows. In practice, the turbulence modeling community uses various properties of the Reynolds stress anisotropy tensor

$$a_{ij} = \frac{\overline{u'_i u'_j}}{2k} - \frac{\delta_{ij}}{3} \ , \ \text{where } k = \frac{\overline{u'_n u'_n}}{2} \ , \tag{1.1}$$

to both inform model development and compare different modeling techniques. At present there are only a handful of visualization techniques for second-order tensor fields, e.g., glyphs or hyperstreamlines (Hashash *et al.* 2003), and none is used broadly by the CFD community due to their complex construction and difficulty of interpretation. Instead a variety of derived quantities, which distill the relevant information contained in a_{ij} to either scalar or vector metrics, are used to investigate anisotropic behavior.

One of the most popular techniques is the use of anisotropy invariant maps. Originally introduced by Lumley & Newman (1977), these maps are two-dimensional domains based on invariant properties of a_{ij}. The diagonalization of a_{ij} provides three eigenvalues (λ_1, λ_2, and λ_3)†, or magnitudes, and three eigenvectors (e_1, e_2, and e_3), or directions, of the turbulence anisotropy. Most invariants and scalar metrics of a_{ij} are functionals of the eigenvalues λ_i; by ignoring the eigenvectors these metrics no longer represent information about the directional distribution. Despite this shortcoming, invariant maps have been used in numerical modeling and both numerical and experimental analyses of a diverse set of fluid flows.

One challenge with broader adoption of invariant maps as an analysis tool is their limited range of applicability. As we will show in Section 2, these domains are only useful for visualizing small amounts of data, and their utility is stunted by a lack of context or

† Defined such that $\lambda_1 \geq \lambda_2 \geq \lambda_3$ and the sum of these eigenvalues is zero.

correlation to the spatial domain. Put differently, information (anisotropy data from a region of the flow) is taken from the spatial domain and visualized in the invariant map. It is hoped that knowledge is gained from this visualization, but the workflow stops at this point.

In this brief we propose a new visualization technique which allows the knowledge and information gained in the invariant map to be represented in the spatial domain, adding an additional transfer of information to the workflow described above. By doing so the utility of the invariant maps is increased because there is no longer a loss of spatial context. In Section 2 we introduce in detail several common invariant maps and describe how they are differentiated. We focus on one in particular, the barycentric map, to define a new visualization technique. Section 3 introduces the new technique, which is subsequently compared against traditional scalar metrics of anisotropy. The visualization approach is demonstrated in Section 4 for three cases: the flow over a random cube array, flow over a wavy-wall channel, and a shock-turbulent boundary layer interaction (STBLI). A simple extension of the approach for visualization of targeted anisotropic behavior is presented in Section 5. The brief concludes by discussing future areas of research based on the results presented.

2. Anisotropy invariant maps

The anisotropy invariant maps (AIMs) described in this section share the common trait that the independent variables x_{AIM} and y_{AIM} axes variables are functions of the anisotropy eigenvalues λ_i. These eigenvalues are used to describe the relative strengths of the fluctuating velocity components, i.e., the componentality of the turbulence field (Helgeland *et al.* 2004). There are three limiting states of componentality which define the boundaries of the invariant maps. All other states of a_{ij} (other locations within the map) can be represented as a convex combination of these limiting states, which are

(a) one-component: describes a flow where turbulent fluctuations only exists along one direction, i.e., when $\lambda_i = \left[\frac{2}{3}, \frac{-1}{3}, \frac{-1}{3}\right]^T$. This state is also referred to as rod-like or cigar-shaped turbulence, a visual description which evokes the one-dimensional nature of this state. This state is represented by $\mathbf{x}_{1\mathrm{C}}$ in all maps;

(b) axisymmetric two-component: describes turbulence where fluctuations exist along two directions with equal magnitude, i.e., $\lambda_i = \left[\frac{1}{6}, \frac{1}{6}, \frac{-1}{3}\right]^T$, also referred to as pancake-like turbulence. This state is represented by $\mathbf{x}_{2\mathrm{C}}$;

(c) isotropic: represents turbulence where all three λ_i are equal to zero, also referred to as spherical turbulence. This state is represented by $\mathbf{x}_{3\mathrm{C}}$.

By joining these points the boundaries of the invariant map are formed, which correspond to additional physical behaviors:

(a) axisymmetric expansion: joins $\mathbf{x}_{1\mathrm{C}}$ and $\mathbf{x}_{3\mathrm{C}}$ and occurs when $0 < \lambda_1 < \frac{1}{3}$ and $\frac{-1}{6} < \lambda_2 = \lambda_3 < 0$;

(b) axisymmetric contraction: joins $\mathbf{x}_{2\mathrm{C}}$ and $\mathbf{x}_{3\mathrm{C}}$, occurring when $\frac{-1}{3} < \lambda_1 < 0$ and $0 < \lambda_2 = \lambda_3 < \frac{1}{6}$;

(c) two-component: exists between $\mathbf{x}_{1\mathrm{C}}$ and $\mathbf{x}_{2\mathrm{C}}$ occurring when $\lambda_1 + \lambda_3 = \frac{1}{3}$ and $\lambda_2 = \frac{-1}{3}$.

A final state of interest is that of plane-strain turbulence, where at least one $\lambda_i = 0$, which exists within the map. A wealth of physical understanding and insight is provided by visualizing the proximity of turbulent anisotropy to these different behaviors.

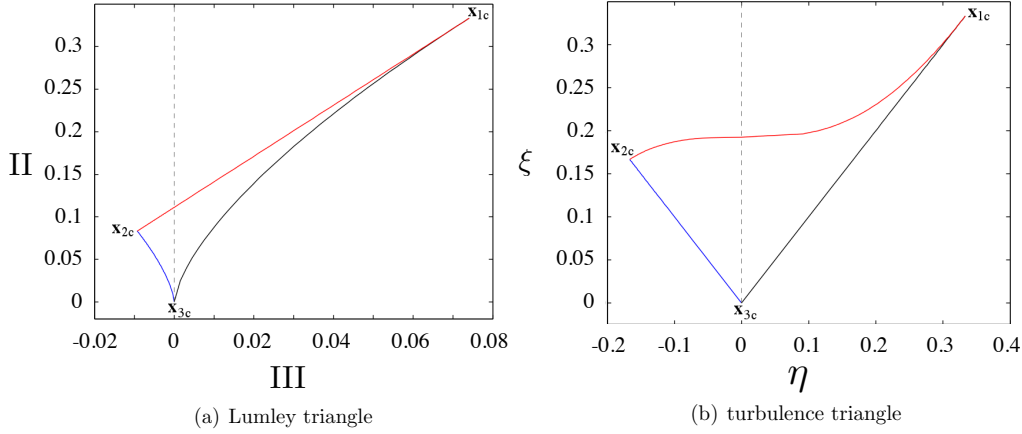(a) Lumley triangle

(b) turbulence triangle

FIGURE 1. Diagram of two non-linear anisotropy invariant maps. The limiting states of componentality are labeled along with the plane-strain limit (dashed line) for reference.

AIMs are typically classified by whether the invariants constituting the axes' variables are non-linear or linear combinations of λ_i. We briefly introduce the four most common invariant maps, two non-linear and two linear domains. We then demonstrate the differences between these maps by visualizing DNS data from turbulent channel flow (Hoyas & Jimenez 2006) in all four maps.

2.1. Non-linear invariant maps

2.1.1. Lumley triangle

The invariant map of Lumley & Newman (1977), also called the Lumley triangle, uses the second and third principal components of turbulence anisotropy (Choi & Lumley 2001; Banerjee *et al.* 2007), defined as

$$II = a_{ij}a_{ji}/2 \quad = \lambda_1^2 + \lambda_1\lambda_2 + \lambda_2^2 , \tag{2.1a}$$

$$III = a_{ij}a_{jn}a_{ni}/3 = -\lambda_1\lambda_2\left(\lambda_1 + \lambda_2\right) , \tag{2.1b}$$

to create the coordinate system (III, II), shown in Figure 1(a).

2.1.2. Turbulence triangle

Another domain based on the invariants II and III, the turbulence triangle uses the coordinate system (η, ξ), where

$$\xi^3 = III/2, \quad \eta^2 = II/3 . \tag{2.2}$$

This mapping, shown in Figure 1(b), stretches the lower left quadrant of the Lumley triangle, providing a detailed view of the region near the isotropic corner. This domain was designed for evaluating trajectories of the return to isotropy of homogeneous turbulence (Choi & Lumley 2001).

2.2. Linear invariant maps

2.2.1. Eigenvalue map

The eigenvalue map simply uses the first and second eigenvalues of the turbulence anisotropy to define the coordinate system (λ_2, λ_1), shown in Figure 2(a).

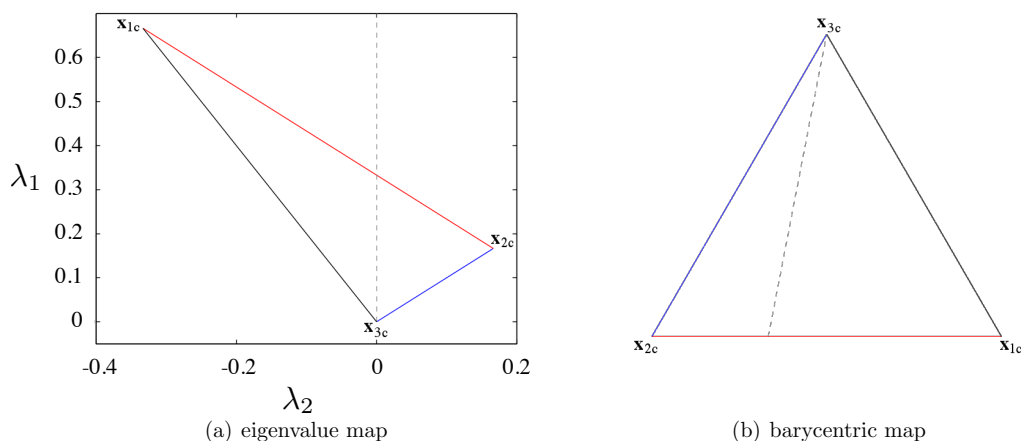*Emory & Iaccarino*

(a) eigenvalue map

(b) barycentric map

FIGURE 2. Diagram of two linear anisotropy invariant maps. The limiting states of componentality are labeled along with the plane-strain limit (dashed line) for reference.

2.2.2. *Barycentric map*

Another construction based on the eigenvalues λ_i, the barycentric map of Banerjee *et al.* (2007) leverages the fact that any realizable state of turbulence is a convex combination of the three limiting states of (corners) componentality. A Euclidian domain is constructed where these limiting states are placed at $\mathbf{x}_{1C} = (1, 0)$, $\mathbf{x}_{2C} = (0, 0)$, and $\mathbf{x}_{3C} = (1/2, \sqrt{3}/2)$. Although these points can be chosen arbitrarily, an equilateral triangle is chosen which equally weights the different limiting states. The coordinate system (x_B, y_B) is defined such that

$$x_B = C_{1c}x_{1c} + C_{2c}x_{2c} + C_{3c}x_{3c} = C_{1c} + C_{3c}\frac{1}{2}\,, \qquad (2.3a)$$

$$y_B = C_{1c}y_{1c} + C_{2c}y_{2c} + C_{3c}y_{3c} = C_{3c}\frac{\sqrt{3}}{2}\,, \qquad (2.3b)$$

and the weights are

$$C_{1c} = \lambda_1 - \lambda_2\,, \qquad (2.4a)$$
$$C_{2c} = 2\left(\lambda_2 - \lambda_3\right)\,, \qquad (2.4b)$$
$$C_{3c} = 3\lambda_3 + 1\,. \qquad (2.4c)$$

Uniqueness within the barycentric map is enforced by the constraint that the sum of the weights $C_{ic} = 1$.

2.3. *Example: turbulent channel flow*

To visualize the differences between these maps we plot a wall-normal profile (extending to the centerline) from DNS of developed turbulent channel flow (Hoyas & Jimenez 2006), shown in Figure 3. The physics of this flow are not discussed here; the focus is on highlighting differences between the visual representations.

In all maps the trajectories initiate at the two-component limit (wall) and move towards the one-component corner before heading towards the isotropic corner (channel centerline). As a general conclusion the non-linear maps appear to bias the profiles towards the axisymmetric expansion boundary relative to the linear maps. Perhaps the most noticeable difference between the non-linear and linear domains is the degree to

(a) Lumley triangle

(b) turbulence triangle
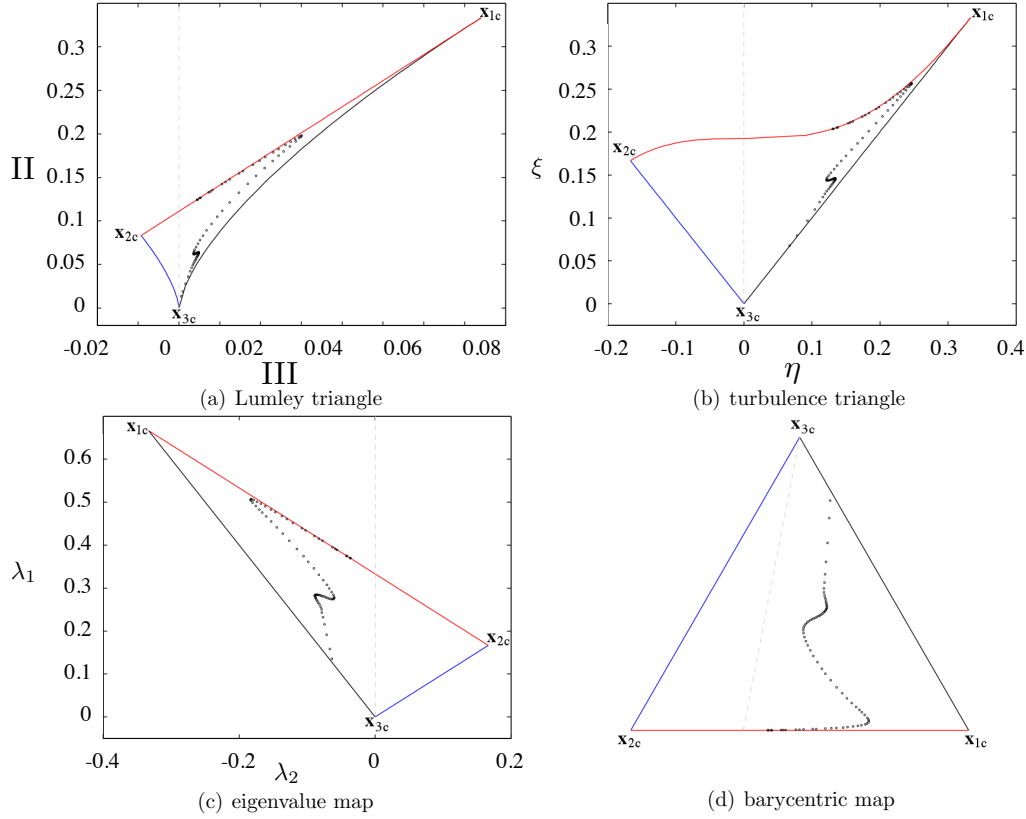
(c) eigenvalue map

(d) barycentric map

FIGURE 3. Turbulent channel flow DNS data (Hoyas & Jimenez 2006) plotted within four anisotropy invariant maps.

which the turbulence approaches the isotropic corner. Based on the non-linear maps, one might assume the turbulence is nearly isotropic at the channel centerline, whereas the linear maps show this to be an incorrect assertion - an observation noted by Banerjee *et al.* (2007).

As was evident in this exercise, even for a very simple flow it is difficult to correlate the trajectories in the AIMs to the spatial domain. The work presented in the rest of the document is an effort to transfer the componentality information learned within the AIMs back to the physical domain. We choose to leverage the barycentric map in particular for this work, primarily because the equal weighting of limiting states provides an intuitive and more easily interpretable result.

2.4. *Limitations of invariant maps*

Qualitatively, the strength of the barycentric map is the ability to convey proximity to limiting states of componentality. While this map (and invariant maps in general) have proven useful for turbulence modeling and analysis of simple flows, there are two significant drawbacks when it is applied to complex flows: (1) the loss of physical context, and (2) difficulty in representing large amounts of data.

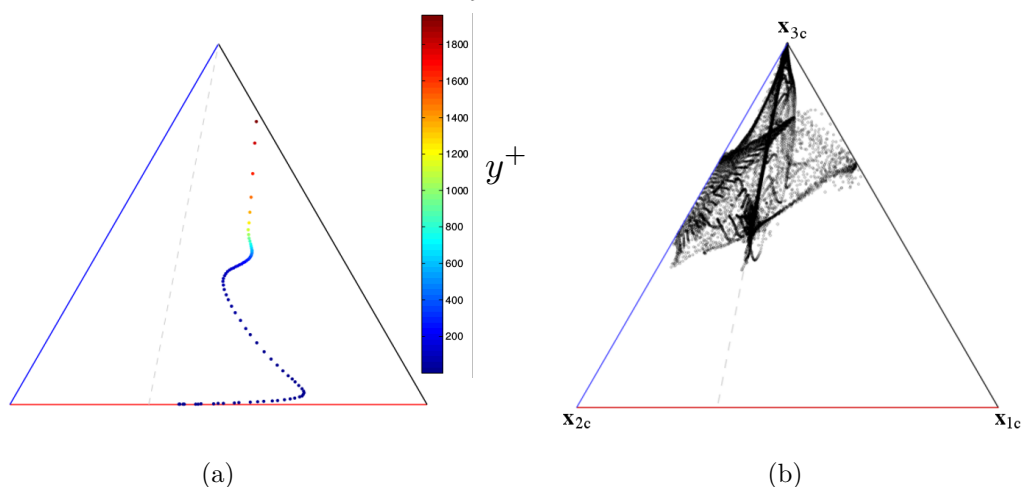(a)   (b)

FIGURE 4. Barycentric maps showing different CFD results data. In (a) the same channel flow data as Figure 3(d) is shown, where the points have been colored by the wall distance y^+. In (b) the entire domain from a contracting-diverging nozzle flow (RANS solution of the Délery C flow (Emory 2014, chap. 4.3)) is plotted.

2.4.1. *Loss of physical context*

Because the invariants used to define (x_B, y_B) in Eq. (2.3) are based only on λ_i, the barycentric map trajectories cannot contain information regarding the physical domain. There have been attempts to address this shortcoming, such as individually labeling the scatter points with spatial coordinates or coloring the points based on physical coordinates. In Figure 4(a) we demonstrate the latter approach, where colors indicate the wall distance y^+. Though this does provide some context, there is a significant burden on the reader/analyst to (a) interpret the colors and (b) map the componentality information back to physical coordinates.

2.4.2. *Large amounts of data*

Complicating the interpretation of the barycentric map is that while each state of anisotropy uniquely maps to a different location within the barycentric map, physical locations with nearly identical a_{ij} will overlap within the barycentric map. This cluttering phenomenon can obscure many data points from the analysis. As the number of points plotted increases, this shortcoming becomes more pronounced; for example Figure 4(b), where the entire domain of a relatively simple flow† has been represented within the barycentric map. Both the obscuring of data points and lack of physical context render this plot nearly useless. For this reason analysts who are investigating large complex flow domains must plot only a subset of the domain information, typically one-dimensional profiles. This limitation makes identification of global componentality behaviors and patterns more difficult.

† Data from the Délery C turbulent channel flow (Délery 1981), which is described in Section 5.

3. Componentality contours

3.1. *Implementation*

We introduce a new visualization technique to represent componentality information in the physical domain by constructing a color map from the barycentric map coordinates (x, y). Color mapping is a common technique for scalar visualization, where the scalar values are used as indices to a lookup table which contains color information (Helgeland 2007).

One of the most common color maps is the red-green-blue (RGB) color system which uses three scalar values, one each for the red, blue, and green color intensities. The values of these three channels must $\in [0, 1]$,† represented as a triplet such that $[1\,0\,0]^T$ is red, $[0\,1\,0]^T$ is green, and $[0\,0\,1]^T$ is blue. All colors can be represented as a linear combination of these triplets.

We make the observation that the coefficients C_{ic}, used to construct the barycentric map coordinates in Eq. (2.3), are similar to an RGB triplet in that they also $\in [0, 1]$. The only notable difference between C_{ic} and an RGB triplet is that the sum of the coefficients must equal one; no such constraint exists for an RGB triplet. We formulate an RGB value using the componentality coefficients to weight the RGB color channels through

$$\begin{bmatrix} R \\ G \\ B \end{bmatrix} = C_{1c} \begin{bmatrix} 1 \\ 0 \\ 0 \end{bmatrix} + C_{2c} \begin{bmatrix} 0 \\ 1 \\ 0 \end{bmatrix} + C_{3c} \begin{bmatrix} 0 \\ 0 \\ 1 \end{bmatrix} . \tag{3.1}$$

This simple construction assigns colors to componentality behaviors such that one-component turbulence is red, two-component is green, isotropic is blue, and all other states within the map are combinations of these colors. In Figure 5(d) we show the barycentric map colored in this approach; this map now serves as a color map with which we can visualize the physical domain and quickly determine proximity to the limiting states of anisotropy.

A variety of scalar anisotropy metrics have been developed as analysis tools, e.g., used to study the diffusion of water within biological tissues (Kindlmann *et al.* 2000; Prados *et al.* 2010). These tools and their associated color maps are inappropriate for representing turbulence componentality. The anisotropy maps demonstrate that componentality is described by two independent parameters; by reducing the anisotropy to a scalar value important information is lost. This is demonstrated in Section 5, a discussion comparing a variety of scalar metrics to componentality contours is provided in Emory (2014, Chapter 2).

3.2. *Invariant map analysis*

The primary use for these contours is flow-field analysis, presented in Section 4 for several cases. Componentality contours can also be used to better understand the differences between the invariant maps discussed in Section 2. We visualize componentality contours in Figure 5 for all four invariant maps, highlighting the differences between their representations of a_{ij}.

Several trends become clear from this comparison. The first is that the Lumley triangle dedicates most of its area to one- and two-component behavior. Second, the turbulence triangle dedicates more of its area to two-component and isotropic turbulence. By minimizing one limiting state, these non-linear maps explore in more detail the interplay

† Technically each value is represented by 8 bits, and thus range from $\in [0, 255]$. In many visualization packages these ranges are normalized to $[0, 1]$.

(a) Lumley triangle

(b) turbulence triangle

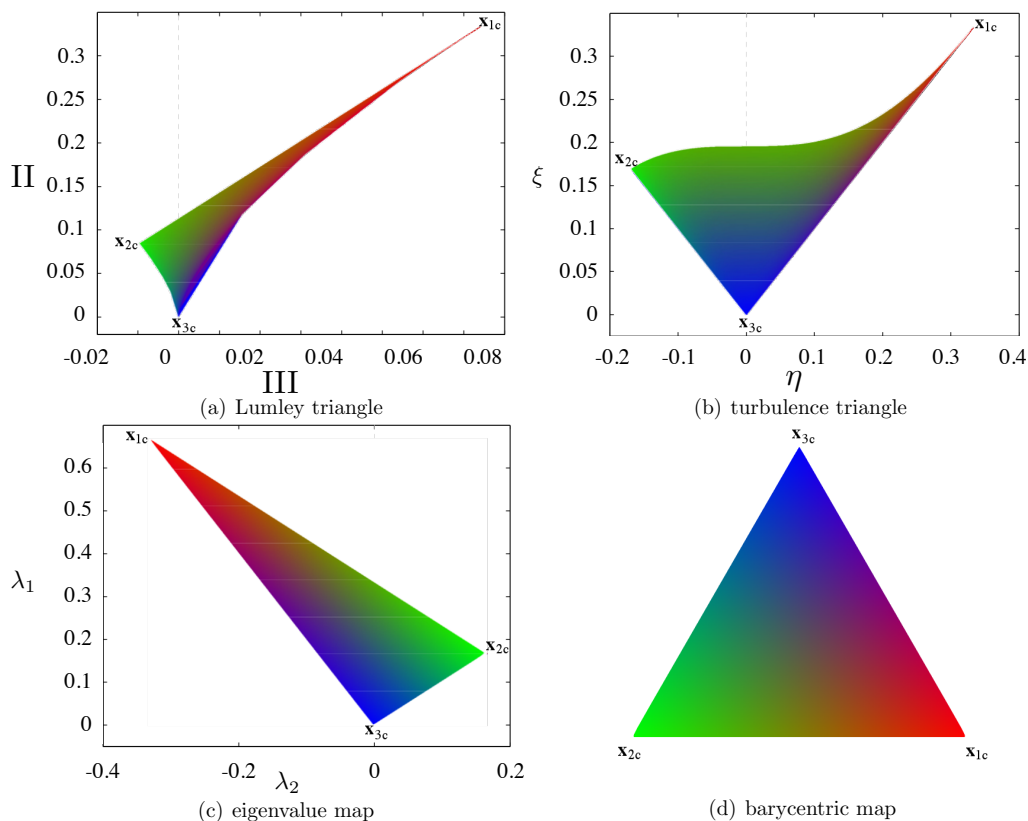(c) eigenvalue map

(d) barycentric map

FIGURE 5. Reynolds stress anisotropy componentality contours plotted in four anisotropy invariant maps.

between the remaining two states. In contrast, the linear maps utilize a more equal weighting of the three limiting states.

4. Examples

We demonstrate application of componentality contours to three cases†, showing their use for both exploration and analysis of complex fluid flow results. The physics of each case will not be discussed in depth. Most of the discussion centers on the analyses enabled by the componentality contour color map.

4.1. *Flow through an urban-like canopy*

The atmospheric boundary layer flow over a building array with variable heights (all buildings have a square planform area) is numerically investigated using large-eddy simulation (LES) by Philips *et al.* (2013). The goal of this work is to study scalar dispersion of a point source within this domain, which is shown in Figure 6. Sensitivity of dispersion to flow direction was evaluated by using three orientations (relative to the x-axis): $0°$, $45°$, and $90°$.

In Figure 7 time-averaged componentality contours are shown for a horizontal slice

† Additional examples can be found in Emory (2014, Figures 2.18 and E.3).
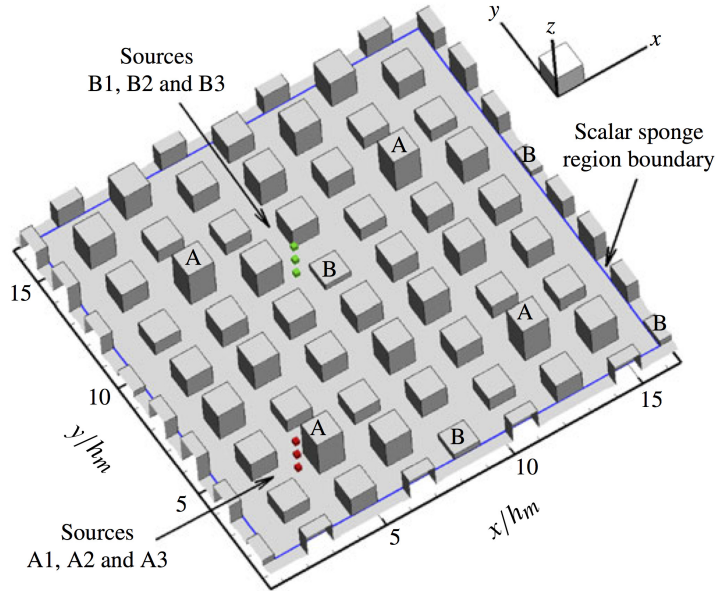
FIGURE 6. Diagram of the variable height building array (Philips *et al.* 2013, Figure 1).

(xy-plane) whose height is equal to that of the largest building (white square). The authors were able to quickly explore the domain as well as qualitatively identify regions of interesting turbulence behavior by visualizing the anisotropy in this way. Looking first at Figure 7(a), the most prominent feature is the wake downstream of the tallest building, which is primarily isotropic (blue coloration). Immediately adjacent to the walls of the tallest building are regions of $\mathbf{x}_{2C}$ turbulence, and as the flow interacts and turns around the corners there is significant $\mathbf{x}_{1C}$ behavior. The top surfaces of the nearby tall buildings (the shorter buildings' influence is not visible in this plane) indicate $\mathbf{x}_{2C}$ behavior; downstream of these buildings the turbulence is near a state of axisymmetric expansion (red-purple hues).

In Figure 7(c) there are banding patterns in the componentality contours. These occur because the buildings are aligned in parallel with respect to the flow direction; the wake structures are allowed to propagate long distances. These striations are not visible in Figure 7(a), where the buildings are staggered relative to the flow. This causes the wake structures to frequently interact with nearby buildings; they can only propagate short distances before being disturbed.

4.2. *Oblique shock-boundary layer interaction*

An oblique shock turbulent boundary layer interaction (OSTBLI) is investigated by Morgan *et al.* (2013). In this work LES results are used to evaluate the performance of several different Reynolds-averaged Navier-Stokes (RANS) turbulence models, specifically the Reynolds stress transport (RST) and $k-\omega$ models. These three turbulence modeling approaches are compared using componentality contours in Figure 9, showing a spanwise plane zooming in on the interaction region (shock location is identified by isobaric lines in black).

The most notable difference between the two RANS models and the LES is the near-wall layer of $\mathbf{x}_{1C}$ turbulence (red coloring) upstream of the interaction. Downstream of
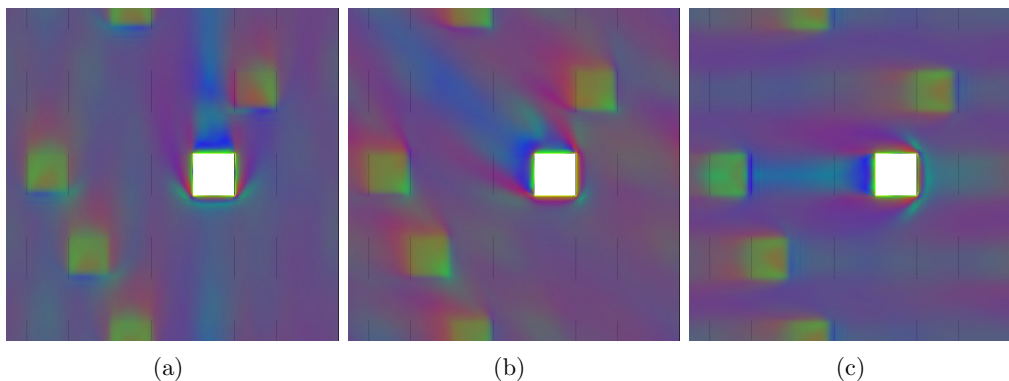
FIGURE 7. Anisotropy componentality contours for a horizontal plane at the height of the tallest building (white square) for one quadrant of the domain. These images correspond to time-averaged LES data (D. Philips, private communication, March 19th, 2012) where the atmospheric boundary layer angle of attack (relative to the x axis) is (a) $0°$, (b) $45°$, and (c) $90°$. Colors indicate componentality where red: one-component; green: axisymmetric two-component; blue: isotropic.
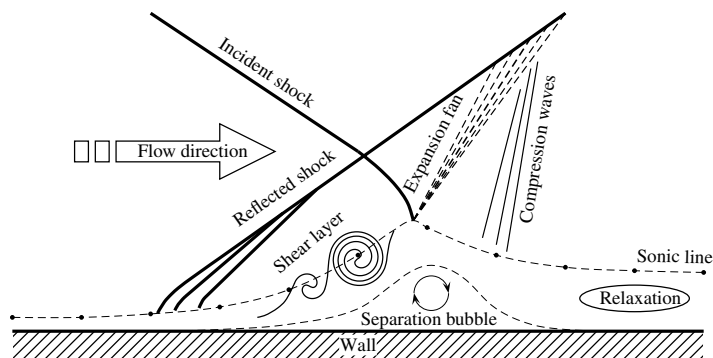

FIGURE 8. Illustration of a typical oblique shock-boundary layer interaction (Morgan *et al.* 2013, Figure 1).

the interaction the LES indicates strong $\mathbf{x}_{2C}$ turbulence adjacent to the wall. While both RANS models do relatively well capturing the pressure field, they fail to predict either the $\mathbf{x}_{1C}$ or $\mathbf{x}_{2C}$ anisotropic behavior near the wall. They predict surprisingly similar anisotropy in this region despite a significant difference in model complexity†.

4.3. *Wavy wall channel*

The turbulent flow in a channel with a sinusoidal (wavy) bottom wall has been investigated using a variety of turbulence simulation techniques (Rossi & Iaccarino 2009; Gorlé *et al.* 2012). The periodic (both streamwise and spawns) domain is shown in Figure 10. A single wavelength of the sinusoidal wall (peak-to-peak) is used to compare the different turbulence simulations.

Figure 11 uses componentality contours to compare DNS, LES, and two RANS models (Philips 2012). The DNS and LES are nearly identical in their prediction of the

† The $k-\omega$ model is a two-equation eddy-viscosity model whereas the RST uses six transport equations, one for each term of the Reynolds stress.
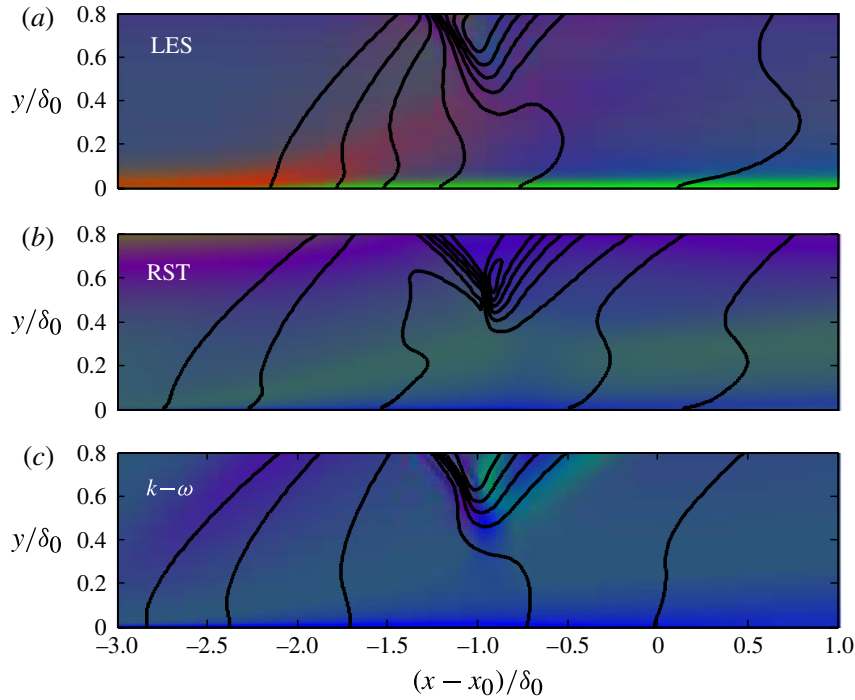
FIGURE 9. Componentality contours for OSTBLI obtained from (a) large-eddy simulation, (b) a Reynolds stress transport model, and (c) and $k-\omega$ eddy-viscosity model. Isobars (black lines) are provided for reference (Morgan *et al.* 2013, Figure 37).
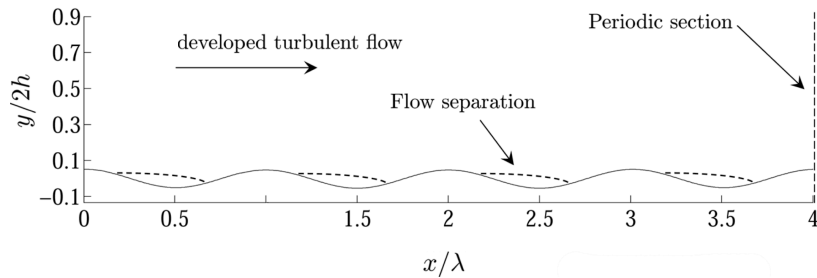

FIGURE 10. Illustration of the wavy wall channel geometry and location of separated flow (Gorlé *et al.* 2012, Figure 1).

anisotropy, showing a layer of $\mathbf{x}_{1C}$ emanating from the peak (where separation occurs). The rest of the sinusoidal wall has a thick layer of $\mathbf{x}_{2C}$ turbulence. The top wall is primarily $\mathbf{x}_{1C}$, whereas the channel core is nearly isotropic. The RST model adequately represents these phenomena, though somewhat underpredicting the extent away from the wall where these behaviors exist. The final RANS model, the v^2-f, shows little resemblance to any of the other results, predicting nearly isotropic turbulence throughout the channel.
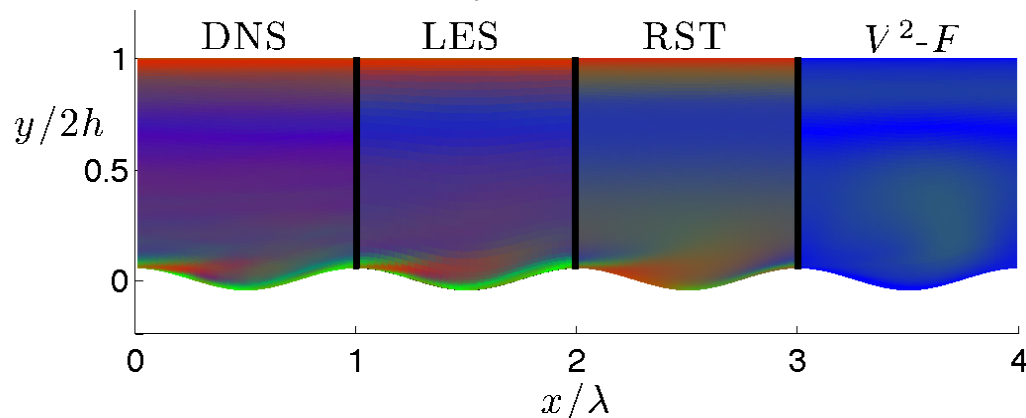
Emory & Iaccarino

FIGURE 11. Comparison of Reynolds stress anisotropy componentality contours for four different simulations of turbulent wavy wall flow (Philips 2012, Figure 5.11).

4.4. *Conclusion*

The fundamental feature of the proposed color map is the ability to visualize the anisotropic behavior of turbulence in the physical domain. The comparisons performed in Figures 11 and 9 would be difficult to interpret if performed only in an invariant map; context with regards to flow features and geometry would be lost. Relative to invariant maps, the same type of information is visualized (componentality of turbulence), but this coloring technique is able to address both the loss of context and quantity of data shortcomings that limit broader use of invariant maps.

5. Alternative coloring schemes

Two extensions to this color map approach are currently being explored. The first is related to an optimal choice of colors which more delineate the different limiting behaviors of componentality. The second introduces a modified formulation of Eq. (3.1) which allows for more complex color maps, enhancing the color maps' ability to highlight limiting behaviors of anisotropy.

5.1. *Modified corner colors*

In Figure 5(d) the RGB base colors (colors at the corners) are defined as $[1\,0\,0]^T$, $[0\,1\,0]^T$, and $[0\,0\,1]^T$, respectively. There is no reason why red, green, and blue must be used at these corners. The analyst may want to use a different set of colors to enhance visual perception of particular limiting states, which requires a trivial modification to the corner colors described in Eq. (3.1). We demonstrate this using contours from a RANS solution of the Délery Case C flow (Délery 1981). This turbulent channel flow has a large bump on the lower wall which causes the flow to accelerate from subsonic conditions to a standing shock of $M \approx 1.4$, which spans the channel. The shock interacts with the turbulent boundary layers on both top and bottom walls, inducing a large separation bubble downstream of the bump geometry. These features are evident in Figure 12(a) which shows Mach contours of this flow.

Figures 12(b) and 12(c) depict the standard RGB componentality color map, while Figures 12(d) and 12(e) show an alternative color map where the base colors have been modified (equivalent to the component anisotropy index scalar metric). Figure 12(d)
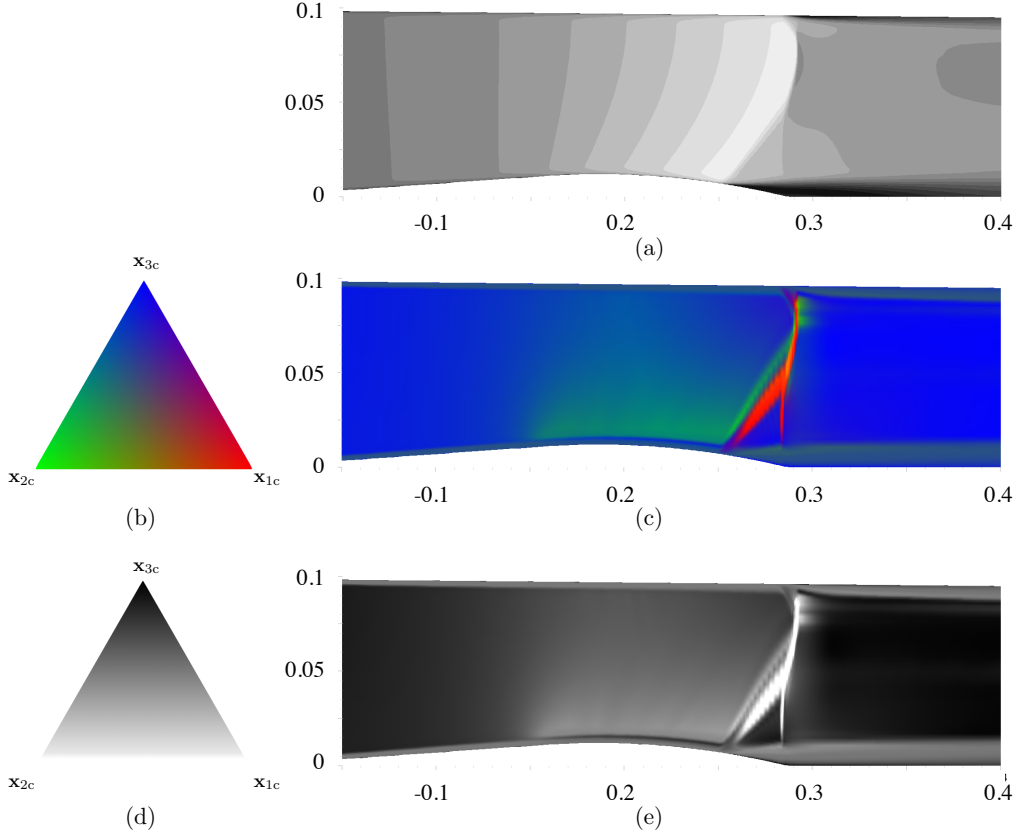
FIGURE 12. Contours for the Délery C flow using the SST model. In (a) Mach contours ($M = 0$: black, $M = 1.4$: white, 15 uniformly speed contours) visualize the shock and separated flow. In (b) and (c) the RGB color map, described by $[1\,0\,0]^T$, $[1\,1\,1]^T$, and $[0\,0\,1]^T$, and associated componentality contours are displayed; in (d) and (e) the modified color map, described by $[1\,1\,1]^T$, $[1\,1\,1]^T$, and $[0\,0\,0]^T$, and associated contours are displayed.

shows that the color map produces a gradient perpendicular to the two-component (bottom wall) limit; indicating distance from the isotropic corner. The limitation of using a scalar metric is evident when comparing Figures 12(c) and 12(e); the white region in Figure 12(e) is non-uniquely specified with this color map.

5.2. *Modified map construction*

While the color maps described by Eq. (3.1) adequately identify behavior very close to the corners of the map, the gradients in the interior and near the edges of the domain are much harder to visually interpret. In order to address this (and allow these color maps to clearly demarcate other regions within the barycentric map), we introduce a new formulation for the RGB channel values

$$\begin{bmatrix} R \\ G \\ B \end{bmatrix} = C_{1c}^* \begin{bmatrix} 1 \\ 0 \\ 0 \end{bmatrix} + C_{1c}^* \begin{bmatrix} 0 \\ 1 \\ 0 \end{bmatrix} + C_{1c}^* \begin{bmatrix} 0 \\ 0 \\ 1 \end{bmatrix} , \qquad (5.1a)$$

where $C_{ic}^* = (C_{ic} + C_{off})^{C_{exp}}$. $\qquad (5.1b)$

(a) $C_{off} = 0.65$, $C_{exp} = 5$

(b) $C_{off} = 0.80$, $C_{exp} = 5$

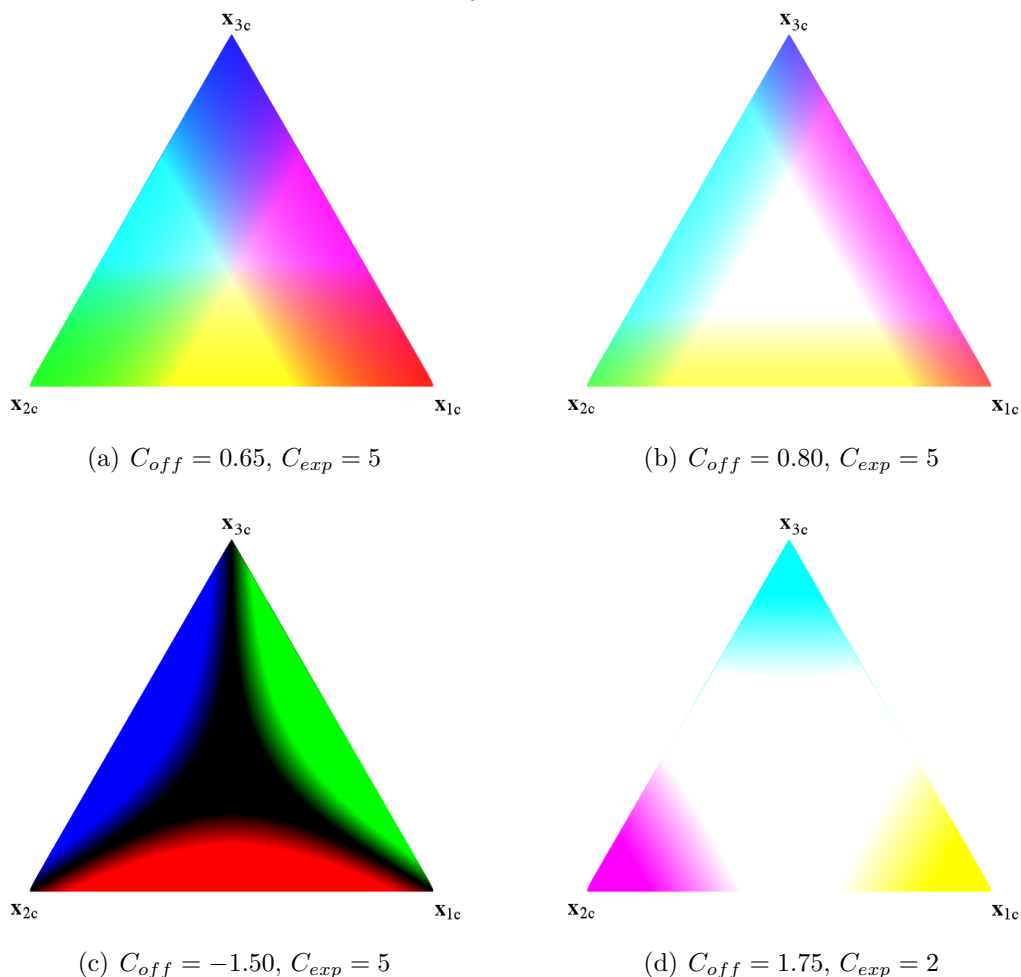(c) $C_{off} = -1.50$, $C_{exp} = 5$

(d) $C_{off} = 1.75$, $C_{exp} = 2$

FIGURE 13. Barycentric map componentality contours using different values for the coefficient offset C_{off} and exponent C_{exp}. In (a) and (b) the RGB base colors are $[1\,0\,0]^T$, $[0\,1\,0]^T$, and $[0\,0\,1]^T$, respectively; in (c) and (d) they are $[0.5\,0.5\,-0.5]^T$, $[0.5\,-0.5\,0.5]^T$, and $[-0.5\,0.5\,0.5]^T$ (corresponds to yellow-magenta-cyan).

By changing the base color regime and modifying the offset and exponent coefficients, several potentially useful color regions can be constructed. For example, in Figures 13(a) and 13(b) the behaviors near the limiting states (corners) are still clearly identified by red, green, and blue. Now, however, states in the interior and near the edges of the map are clearly identified with their own colors. In Figure 13(b) only behaviors near the boundaries† are identified; states of anisotropy which correspond to the middle of the barycentric map are not colored at all. The map in Figure 13(c) is used to identify only behaviors near the edges of the map (neglecting corner proximity), and the inverse which only focuses on proximity to corners is demonstrated in Figure 13(d).

† The thickness of this layer is controlled by C_{off}; the smoothness of the color map transition from colored to white is controlled by C_{exp}.

6. Conclusion and future work

This brief has described the development and use of a new color map based on turbulence anisotropy componentality. The color map is an extension of anisotropy invariant maps and allows information about componentality to be plotted in physical dimensions. This coloring technique provides analysts with a faster and more intuitive visualization of the anisotropic behavior of an arbitrary second-order tensor which maintains physical context and can handle large amounts of data (relative to invariant maps). Several extensions to this coloring approach were presented which allow for targeted coloring of physical behaviors.

Future work involves further application of this coloring approach to complex flows, demonstrating the utility of these visualizations. Additionally the alternative coloring schemes will be explored and refined in terms of their ability to enhance our physical understanding of flow physics and their impact on modeling approaches.

REFERENCES

BANERJEE, S., KRAHL, R., DURST, F. & ZENGER, C. 2007 Presentation of anisotropy properties of turbulence, invariants versus eigenvalue approaches. *J. Turbul.* **8**, 1–27.

CHOI, K. & LUMLEY, J. 2001 The return to isotropy of homogeneous turbulence. *J. Fluid Mech.* **436**, 59–84.

DÉLERY, J. 1981 Investigation of strong shock turbulent boundary layer interaction in 2D transonic flows with emphasis on turbulence phenomena. In 14th *AIAA Fluid and Plasma Dynamics Conference*.

DUBIEF, Y. & DELCAYRE, F. 2000 On coherent-vortex identification in turbulence. *J. Turbul.* **1** (11).

EMORY, M. A. 2014 *Estimating model-form uncertainty in Reynolds-averaged Navier-Stokes closures.* PhD Thesis, Stanford University.

GORLÉ, C., EMORY, M., LARSSON, J. & IACCARINO, G. 2012 Epistemic uncertainty quantification of RANS modeling of the flow over a wavy wall. *Annual Research Briefs*, Center for Turbulence Research, Stanford University, pp. 81–91.

HASHASH, Y., YAO, J. & WOTRING, D. 2003 Glyph and hyperstreamline representation of stress and strain tensors and material constitutive response. *Int. J. Numer. Anal. Met.* **27**, 603–626.

HELGELAND, A. 2007 *3D texture-based flow visualization.* PhD Thesis, University of Olso.

HELGELAND, A., ANDREASSEN, O., OMMUNDSEN, A., REIF, B. & WERNE, J. 2004 Visualization of the energy-containing turbulent scales. In *IEEE Symposium on Volume Visualization and Graphics*, pp. 103–109.

HOYAS, S. & JIMENEZ, J. 2006 Scaling of the velocity fluctuations in turbulent channels up to $Re_\tau = 2003$. *Phys. Fluids* **18**, 011702.

KINDLMANN, G., WEINSTEIN, D. & HART, D. 2000 Strategies for direct volume rendering of diffusion tensor fields. In *IEEE T. Vis. Comput. Gr.*, vol. 6.

Lumley, J. & Newman, G. 1977 The return to isotropy of homogenous turbulence. *J. Fluid Mech.* **82**, 161–178.

Morgan, B., Duraisamy, K., Nguyen, N., Kawai, S. & Lele, S. 2013 Flow physics and RANS modeling of oblique shock/turbulent boundary-layer interaction. *J. Fluid Mech.* **729**, 231–284.

Philips, D., Rossi, R. & Iaccarino, G. 2013 Large-eddy simulation of passive scalar dispersion in an urban-like canopy. *J. Fluid Mech.* **723**, 404–428.

Philips, D. A. 2012 *Modeling scalar dispersion in urban environments.* Ph.D. thesis, Stanford University.

Prados, F., Boada, I., Prats-Galino, A., Martin-Fernandez, J., Feixas, M., Blasco, G., Puig, J. & Pedraza, S. 2010 Analysis of new diffusion tensor imaging anisotropy measures in the three-phase plot. *J. Magn. Reson. Imaging* **31**, 1435–1444.

Rossi, R. & Iaccarino, G. 2009 Numerical simulation of scalar mixing from a point source over a wavy wall. *Annual Research Briefs*, Center for Turbulence Research, Stanford University, pp. 453–464.

Van Dyke, M. 1982 *An album of fluid motion*, 10th ed., Parabolic Press.